Application of the inverse scattering imaging condition in least-squares migration and full waveform inversion

Natiê Almeida Albano* (UFPA), Jessé Carvalho Costa (UFPA)

Abstract

We present an efficient preconditioning of least squares reverse time migration (LSRTM) based on the inverse scattering image condition (ISIC). Numerical experiments using the Marmousi II model validate our approach in the data and in the image domain. Moreover, we show a modification of ISIC to promote the reflected tomographic components of the wavefield for full waveform inversion (FWI). This result accelerates the convergence of FWI, even when the spectrum of the recorded wavefield does not have low-frequency energy, and inverts more accurate velocity models.

Introduction

Migration and inversion of the full wavefield are two of the most commonly used methodologies in the seismic prospecting process. Migration aims to estimate subsurface structures using different techniques. Among them, reverse time migration (RTM) has been widely employed since the 1990s due to its ability to imaging models with complex structures effectively. However, the amplitudes obtained in the migrated image do not accurately with the true amplitude of the subsurface reflection coefficients.

Aiming to produce migrated images with amplitudes relative to the true reflection coefficients, Kiyashchenko et al. (2007) and Op't Root et al. (2012) proposed the inverse scattering imaging condition (ISIC). In a more detailed mathematical study using microlocal analysis, Op't Root et al. (2012) demonstrated that this image condition is an asymptotic inverse of the linearized scalar acoustic wave equation (Born approximation). The numerical implementation of ISIC in the time domain needs two cross-correlation terms, one relative to the time derivatives of the source and receiver wavefields and the other to the gradients of those same wavefields. This leads to a higher computational cost compared to implementing the Claerbout image condition with the Laplacian filter and illumination compensation (CLI).

Albano et al. (2023), using high-frequency approximation and redistributing the frequency factors present in the original equation of Op't Root et al. (2012), derive several alternative expressions for the ISIC implementation. Two of these approaches, similar to Douma et al. (2010),

depend on the Laplacian operator and only one cross-correlation term resulting in the same implementational cost as the CLI. However, effects such as limited aperture of the acquisition array, variations in model illumination, and limited frequency band of the source can affect the quality of the migrated image regardless of the imaging condition used. To mitigate these issues the migration is formulated as a linear inverse problem (least-squares migration - LSM), Nemeth et al. (1999); Trad* (2015); Dai and Schuster (2009).

On the other hand, Full Waveform Inversion (FWI) is a non-linear inversion method that aims to estimate the properties of the background medium through which the wavefields propagate (Tarantola, 1984; Pratt and Worthington, 1990; Sirgue et al., 2009; Warner et al., 2013). Although the formulation of the FWI considers that full information from the seismogram can be used in the inversion process, the presence of lower frequency content as possible in the data, and an initial model not too far from the true one avoids cycle skipping and solution stagnation at local minima, Shin and Min (2006).

Sirgue (2006) show that the penetration depth of transmitted wavefields depends on the offset between sources and receivers. The greater the offset, the greater the depth of penetration of these events. On the other hand, transmitted wavefields resulting from very long offsets exhibit strong nonlinearity concerning perturbations in the background model. Therefore, reflection tomographic components constitute a relevant source of information for updating the background model in the deeper regions.

In this context, Ramos-Martinez et al. (2016) proposed a robust gradient for FWI that combines the energies of reflected and transmitted wavefields into a single inversion scheme. To achieve this, the authors use the velocity sensitivity kernel of the inversion problem as the search direction. Apart from the sign reversal between the cross-correlation terms, this gradient is similar to ISIC.

In this research, propose a efficient preconditioning least-squares reverse time migration basead on ISIC. Additionally, we modified inverse scattering imaging condition to promote the reflected tomographic components of the wavefield for FWI.

Inverse scattering imaging condition

In this research, we considered the inverse scattering image condition (ISIC) proposed by Op't Root et al. (2012). These authors originally formulated ISIC in the frequency domain as follows,

$$I_r(\mathbf{x}) = \frac{1}{2\pi} \sum_s \int_\omega d\omega \frac{1}{(-i\omega)P_s\overline{P_s}} \left[\overline{P_s}P_r - \frac{c^2(\mathbf{x})}{\omega^2}\nabla\overline{P_s} \cdot \nabla P_r \right] , \quad (1)$$

where $P_s = P_s(\omega, \mathbf{x}; \mathbf{x}_s)$ and $P_r = P_r(\omega, \mathbf{x}; \mathbf{x}_s)$ are, respectively, the Fourier transforms of the source and receiver wavefields, and $c(\mathbf{x})$ is the propagation velocity of the P-wave. Additionally, the bar above the symbols denotes the complex conjugate operation.

To satisfy the image condition 1, the reverse wavefield (P_r), in the time domain (p_r), is backpropagated using the wave equation.

$$\frac{1}{c^2(\mathbf{x})}\frac{\partial^2 p_r(\mathbf{x},t)}{\partial t^2} - \nabla^2 p_r^2(\mathbf{x},t) = F_{d_{obs}}(\mathbf{x}_r,t), \qquad (2)$$

Where $F_{d_{obs}}(\mathbf{x}_r,t)$ denotes a filtered version of the observed data injected at the receiver positions $\mathbf{x}_r$. According to Op't Root et al. (2012), the filtering operation can be represented by

$$F_{d_{obs}}(\mathbf{x}_r,t) = F_B d_{obs}(\mathbf{x},t). \qquad (3)$$

In equation 3, $d_{obs}(\mathbf{x},t)$ represents the observed data and F_B is a boundary operator defined by,

$$F_B = -2iD_t \frac{1}{c(\mathbf{x})}\sqrt{1 - c^2(\mathbf{x})D_t^2 D_{\mathbf{x}}^2}, \qquad (4)$$

com

$$D_t = -i\partial_t \quad \text{e} \quad D_{\mathbf{x}} = -i\partial_{\mathbf{x}}. \qquad (5)$$

Based on equation 1, Albano et al. (2023) derived different implementational forms of ISIC in the time domain. Here, we highlight two of these formulations. The first one is governed by the following expression,

$$I_r(\mathbf{x}) = \sum_s \frac{1}{P'(\mathbf{x},\mathbf{x}_s)}\int_t dt \left[\dot{p}_s\dot{q}_r + c^2(\mathbf{x})\nabla p_s \cdot \nabla q_r\right], \qquad (6)$$

with $ps = ps(t,\mathbf{x};\mathbf{x}_s)$ and $qr = qr(t,\mathbf{x};\mathbf{x}_r)$. The dot above the symbols denotes temporal derivation, and q_r represents temporal integration of the receiver wavefield.

$$q_r(t,\mathbf{x};\mathbf{x}_s) = \int_0^t p_r(t',\mathbf{x};\mathbf{x}_s)\,dt', \qquad (7)$$

and the illumination compensation factor $P'(\mathbf{x},\mathbf{x}_s)$ is evaluated through the autocorrelation of the temporal derivative of the source wavefield, i.e.,

$$P'(\mathbf{x},\mathbf{x}_s) = \int_t dt(\dot{p}_s(t,\mathbf{x};\mathbf{x}_s))^2. \qquad (8)$$

Equation 6 depends on the evaluation of two cross-correlation terms, one between the temporal derivatives of the source and receiver wavefields and the other between the gradients of these same wavefields. In another approach, ISIC is formulated in terms of the Laplacian operator as follows,

$$I_r(\mathbf{x}) = \sum_s \frac{c^2(\mathbf{x})}{2R(\mathbf{x},\mathbf{x}_s)}\nabla^2 \int_t dt \left[r_s(t,\mathbf{x};\mathbf{x}_s)q_r(t,\mathbf{x};\mathbf{x}_s)\right]. \qquad (9)$$

where $r_s(t,\mathbf{x};\mathbf{x}_s)$ represents the second temporal derivative of the source wavefield.

$$r_s(t,\mathbf{x};\mathbf{x}_s) = \frac{\partial^2 p_s}{\partial t^2}, \qquad (10)$$

and $R(\mathbf{x};\mathbf{x}_s)$ is the illumination compensation factor defined as,

$$R(\mathbf{x};\mathbf{x}_s) = \int_t dt(r_s(t,\mathbf{x};\mathbf{x}_s))^2. \qquad (11)$$

As discussed in Albano et al. (2023), the implementation forms of ISIC in equations 6 and 9 are theoretically equivalent and yield numerically approximate results. Both formulations provide migrated images with amplitudes relative to the true reflection coefficients. However, due to the dependence on the evaluation of temporal and spatial derivatives of the source and receiver wavefields, the formulation based on equation 6 requires higher computational cost compared to the numerical implementation of equation 9. In comparison, the computational cost of ISIC in equation 9 is similar to that required for implementing imaging condition of Claerbout (1971) with Laplacian filter and illumination compensation (CLI),

$$I(\mathbf{x}) = \sum_s \frac{1}{P(\mathbf{x};\mathbf{x}_s)}\nabla^2 \int_t dt \left[p_s(t,\mathbf{x};\mathbf{x}_s)p_r(t,\mathbf{x};\mathbf{x}_s)\right] \qquad (12)$$

where the illumination compensation term $P(\mathbf{x};\mathbf{x}_s)$ is given by,

$$P(\mathbf{x};\mathbf{x}_s) = \int_t dt(p_s(t,\mathbf{x};\mathbf{x}_s))^2. \qquad (13)$$

Although the CLI image condition (equation 12) provides migrated images without backscattering noise and efficiently estimates subsurface structures, it does not have the same property as ISIC in achieving amplitudes relative to the true reflection coefficients.

Least Squares Reverse time migration based on the ISIC

The demand for Least Squares Migration (LSM) arises from the fact that the migration operator is the adjoint, and not the inverse, of the modeling operator, resulting in a blurred representation of subsurface reflectivity (Claerbout, 1992). In this image, the resolution is controlled by acquisition parameters (source signature and acquisition geometry) and the physical properties of the medium (Valenciano et al., 2015). Therefore, LSM aims to mitigate these effects and improve the resolution of migrated images.

In the forward problem, it is considered that the modeled data $\mathbf{d}$ is the result of applying a linear modeling operator $\mathbf{L}$ to the reflectivity of the medium $\mathbf{m}$ (Snieder and Trampert, 1999), i.e.,

$$\mathbf{d} = \mathbf{Lm}. \qquad (14)$$

In turn, the application of the adjoint operator $\mathbf{L}^T$ to the observed data set $\mathbf{d}^{obs}$ defines the migration operation as follows,

$$\mathbf{L}^T\mathbf{d}_{obs} = \mathbf{m}_{mig}. \qquad (15)$$

where $\mathbf{m}_{mig}$ is the migrated image. In an initial approach, the inverse problem can be formulated based on the objective function that measures the squared misfit between the observed reflected data ($\mathbf{d}_{obs}$) and the modeled data, i.e.,

$$J(\mathbf{m}) = \|\mathbf{Lm} - \mathbf{d}_{obs}\|^2, \qquad (16)$$

In which, at each iteration, the optimization algorithm seeks to determine a reflectivity model $\mathbf{m}$ capable of minimizing

the residual between the data. According to Menke (1989), the solution to the linear seismic inversion least squares problem 14 that minimizes the quadratic misfit function 16 is defined as follows

$$\mathbf{L}^T\mathbf{L}\mathbf{m} = \mathbf{L}^T\mathbf{d}. \qquad (17)$$

Since $\mathbf{L}^T\mathbf{L}$ has an inverse, equation 17 can be rewritten as,

$$\mathbf{m} = (\mathbf{L}^T\mathbf{L})^{-1}\mathbf{L}^T\mathbf{d}. \qquad (18)$$

Considering the Gauss-Newton approximation of the Hessian matrix of the objective function 16, $\mathbf{L}^T\mathbf{L} = \mathbf{H}$, and the equation that defines the migrated image (equation 15) the least-squares solution 18 can also be defined as,

$$\mathbf{m} = \mathbf{H}^{-1}\mathbf{m}_{mig}. \qquad (19)$$

Equation 18 solves the linear system by iteratively evaluating the modeling operator $\mathbf{L}$ and its adjoint $\mathbf{L}^T$. This methodology is known as least-squares migration in the data domain (Nemeth et al., 1999; Duveneck et al., 2021). On the other hand, equation 19 governs the implementation of LSM in the image domain (Guitton, 2004; Valenciano, 2008; Guo and Wang, 2020).

The evaluation of the modeling and migration operators through the full-wave equation results in least squares reverse time migration (LSRTM). The acoustic approach with constant density is based on the following wave equation,

$$\frac{1}{c^2(\mathbf{x})}\frac{\partial^2 p(t,\mathbf{x})}{\partial t^2} - \nabla^2 p(t,\mathbf{x}) = s(t,\mathbf{x}), \qquad (20)$$

where $s(t,\mathbf{x})$ is the source term. Equation 20 presents a nonlinear relationship between perturbations in the model parameters ($\delta c(\mathbf{x})$) and the wavefield $p(t,\mathbf{x})$. The propagation of the scattered primary wavefield $\delta p(t,\mathbf{x})$ in a scattering model $m(\mathbf{x}) = \frac{2\delta c(\mathbf{x})}{c(\mathbf{x})}$ can be evaluated through the linearization (Born approximation) of the acoustic wave equation 20, i.e.,

$$\frac{1}{c^2(\mathbf{x})}\frac{\partial^2 \delta p(t,\mathbf{x})}{\partial t^2} - \nabla^2 \delta p(t,\mathbf{x}) = \frac{m(\mathbf{x})}{c(\mathbf{x})^2}\frac{\partial^2 p(t,\mathbf{x})}{\partial t^2}. \qquad (21)$$

data-domain least squares reverse time migration

The data-domain least squares reverse time migration (DD-LSRTM) aims to iteratively estimate the solution 18 that minimizes the misfit function between the observed reflected data ($\mathbf{d}_{obs}$) and the modeled scattered data ($\mathbf{d}_{mod}$) using the $l2$ norm, i.e.,

$$J(\mathbf{m}) = \frac{1}{2}\sum_{\mathbf{x}_s}\sum_{\mathbf{x}_r}\|\mathbf{d}_{obs} - \mathbf{d}_{mod}\|^2. \qquad (22)$$

The solution 18 is updated at each iteration k using the iterative solution (Schuster and Liu, 2019).

$$\mathbf{m}_{(k+1)} = \mathbf{m}_{(k)} + \alpha\nabla J_k(\mathbf{m}). \qquad (23)$$

The gradient of the objective function $\nabla J_k(\mathbf{m})$ is constructed by reverse-time injection of the residual between the data at the receiver positions. The iterative process aims to update the reflectivity model by taking a step α in the direction of decreasing gradient.

In DD-LSRTM, the gradient of the objective function is defined by the expression.

$$\nabla J(\mathbf{m}) = -\sum_{\mathbf{x}_s}\frac{1}{c^2(\mathbf{x})}\int_0^T dt\left[p_r(t,\mathbf{x})\frac{\partial^2 p(t,\mathbf{x})}{\partial t^2}\right], \qquad (24)$$

which states that the gradient of the objective function 24 is calculated through the zero-lag cross-correlation between the second temporal derivative of the source wavefield $p(t,\mathbf{x})$ and the adjoint wavefield $p_r(t,\mathbf{x})$ evaluated through the following adjoint wave equation,

$$\frac{1}{c^2}\frac{\partial^2 p_r(t,\mathbf{x})}{\partial t^2} - \nabla^2 p_r(t,\mathbf{x}) = \sum_{\mathbf{x}_r}\left[d_{obs}(t,\mathbf{x}) - d_{mod}(t,\mathbf{x})\right]\delta(\mathbf{x} - \mathbf{x}_r), \qquad (25)$$

where the source term is the residual between the observed and calculated data injected at the receiver positions and back-propagated in time.

Image-domain least squares reverse time migration

The implementation scheme of image-domain least-lquares reverse time migration (ID-LSRTM) is derived from the matrix relation 19 and can also be written as follows

$$\mathbf{m}_{mig} = \mathbf{H}\mathbf{m}. \qquad (26)$$

Equation 26 shows that the migrated image $\mathbf{m}_{mig}$ results from the convolutional relationship between the subsurface reflectivity $\mathbf{m}$ and the Hessian matrix $\mathbf{H}$. In other words, the migrated image corresponds to a filtered version of the true reflectivity where the Hessian matrix acts as a blurring filter (Valenciano, 2008). Given the migrated image and an approximation for the Hessian matrix, the linear system 26 is iteratively solved by minimizing the objective function

$$J(\mathbf{m}) = \|\mathbf{H}\mathbf{m} - \mathbf{m}_{mig}\|^2. \qquad (27)$$

In this research, we approximate each column of the Hessian matrix using the Point Spread Function (PSF), similar to the approach used in Valenciano (2008), Fletcher et al. (2016), Osorio et al. (2021).

Preconditioning LSRTM with ISIC

Considering that the inverse scattering image condition produces migrated images relative to the true reflection coefficients, we propose to use it in the LSRTM workflow to precondition the inversion process. To avoid increasing computational costs, we adopt the formulation based on equation 9. In the data domain application, we use the ISIC as the search direction for updating the reflectivity model. On the other hand, in the image domain approach, we use the inverse scattering image condition to estimate the Point Spread Functions (PSFs) and the migrated image.

Full waveform inversion based on modified ISIC

Full Waveform Inversion (FWI) is a nonlinear seismic inversion method that aims to estimate the properties of the background medium using the complete wave equation. Similar to LSM, the objective function $J(\mathbf{c})$ of the problem consists of minimizing the quadratic norm of the residual between the observed data set $p_{obs}(\mathbf{x}r,t)$ and the modeled

data $p_{mod}(\mathbf{x}_r, t)$.

$$J(\mathbf{c}) = \sum_{\mathbf{x}_s} \sum_{\mathbf{x}_r} \frac{1}{2} \|p_{obs}(\mathbf{x}_r, t) - p_{mod}(\mathbf{x}_r, t)\|^2. \quad (28)$$

In acoustic FWI with constant density, the calculated data is obtained through the numerical solution of the wave equation 20. The minimization of the data misfit function 28 is performed starting from an initial velocity model $\mathbf{c}0$. At each iteration k, the optimization algorithm seeks to update the velocity model $\mathbf{c}_{k+1}$ by taking a step α in the direction of the search $\delta\mathbf{c}_k$ (Virieux et al., 2017).

$$\mathbf{c}_{k+1} = \mathbf{c}_k + \alpha \delta\mathbf{c}_k. \quad (29)$$

In a simpler approach, the search direction $\delta\mathbf{c}_k$ is defined directly by the gradient of the objective function 28, expressed as

$$\nabla J(\mathbf{c}) = -\sum_{\mathbf{x}_s} \frac{2}{c^3(\mathbf{x})} \int_0^T dt \left[p_r(t, \mathbf{x}) \frac{\partial^2 p_s(t, \mathbf{x})}{\partial t^2} \right], \quad (30)$$

where the wavefield $p_r(t, \mathbf{x})$ is evaluated through the following adjoint wave equation,

$$\frac{1}{c^2(\mathbf{x})} \frac{\partial^2 p_r(\mathbf{x}, t)}{\partial t^2} - \nabla^2 p_r(\mathbf{x}, t) = [p_{obs}(\mathbf{x}_r, t) - p_{mod}(\mathbf{x}_r, t)]. \quad (31)$$

The source term in equation 31 refers to the residual of the data injected at the receiver positions in reverse time. In order to attenuate the geometric spreading effect of the source in the deep part of the model, the gradient of the objective function 30 is often preconditioned with a diagonal approximation of the Hessian matrix, known as the pseudo-Hessian matrix. For the scalar acoustic problem, the pseudo-Hessian matrix is defined as (Carneiro et al. (2018)),

$$\mathbf{H}_{ps}(\mathbf{c}) = \sum_{\mathbf{x}_s} \left(\frac{-2}{c^3(\mathbf{x})} \right)^2 \int_0^T dt \left[\frac{\partial^2 p_s(t, \mathbf{x})}{\partial t^2} \frac{\partial^2 p_s(t, \mathbf{x})}{\partial t^2} \right]. \quad (32)$$

Search direction based on modified ISIC

When inverting the sign of the reverse scattering imaging condition 6, we obtain,

$$I_r(\mathbf{x}) = \sum_s \frac{1}{P'(\mathbf{x}, \mathbf{x}_s)} \int_t dt \left[\dot{p}_s \dot{q}_r - c^2(\mathbf{x}) \nabla p_s \cdot \nabla q_r \right]. \quad (33)$$

EExcept for the propagation of the integral of the receiver wavefield and the illumination compensation factor inherent to ISIC, equation 33 is similar to the robust gradient of FWI based on the velocity sensitivity kernel proposed by Ramos-Martinez et al. (2016). Figure 1 compares the gradients of FWI 30 preconditioned with the pseudo-Hessian matrix (Figure 1a) with the gradient based on the modified ISIC 33 (Figure 1b). Comparing the isochrones indicated by the red arrows, we note that although the gradient based on the modified ISIC still exhibits migration components, their amplitudes are smaller than those observed in the gradient of conventional FWI preconditioned with the pseudo-Hessian matrix. Additionally, the reflection tomography component has a higher amplitude in the gradient based on the modified ISIC, as indicated by the blue arrows. Therefore, we propose to precondition the FWI with more information from the reflection tomography components using the gradient based on the modified ISIC 33.
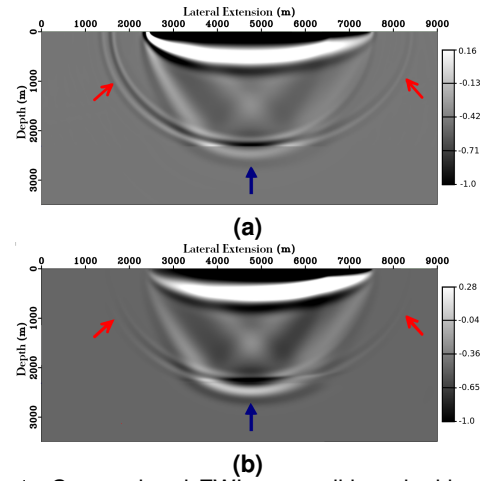

Figure 1: Conventional FWI preconditioned with pseudo-Hessian matrix (a) and the gradient based on modified ISIC (b). The red arrows indicate the migration components, while the blue arrows indicate the reflection tomography components.

Numerical experiments

We evaluated the results of applying ISIC in the LSRTM and modified ISIC in the FWI through numerical experiments involving synthetic data from the Marmousi II velocity model.

Application in LSRTM

Figure 2 shows the results achieved by ISIC-based LSRTM in both the image domain and the data domain (Figures 2e and 2f). For comparison, we also show the corresponding results of conventional LSRTM (Figures 2b and 2c).

The results show that both the conventional LSRTM and the ISIC-based LSRTM converged to approximate models. However, the ISIC-based inversion demonstrates a higher convergence rate, as shown in Figure 3. The black rectangles in the inverted models highlight that the image-domain approach (which requires lower computational cost) provides better results.

Application in FWI

In this experiment, we used a Ricker wavelet with a peak frequency of 8Hz and a frequency spectrum between 3Hz to 15Hz to simulate the observed data through the propagation of the acoustic wave equation with constant density. The velocity models recovered based on the conventional FWI gradient preconditioned with the pseudo-Hessian and the the modified ISIC are presented in Figures 4c and 4d, respectively. The results show that the inversion using the modified ISIC provided a model with higher resolution, especially in the deeper region. This result can be observed in Figure 5, which shows that the approach based on the modified ISIC provides a greater decrease in the objective function.

speed

Conclusion

Our research evaluated the effects of applying the Inverse Scattering Imaging Condition on the recovery of reflectivity

(a)

(c)
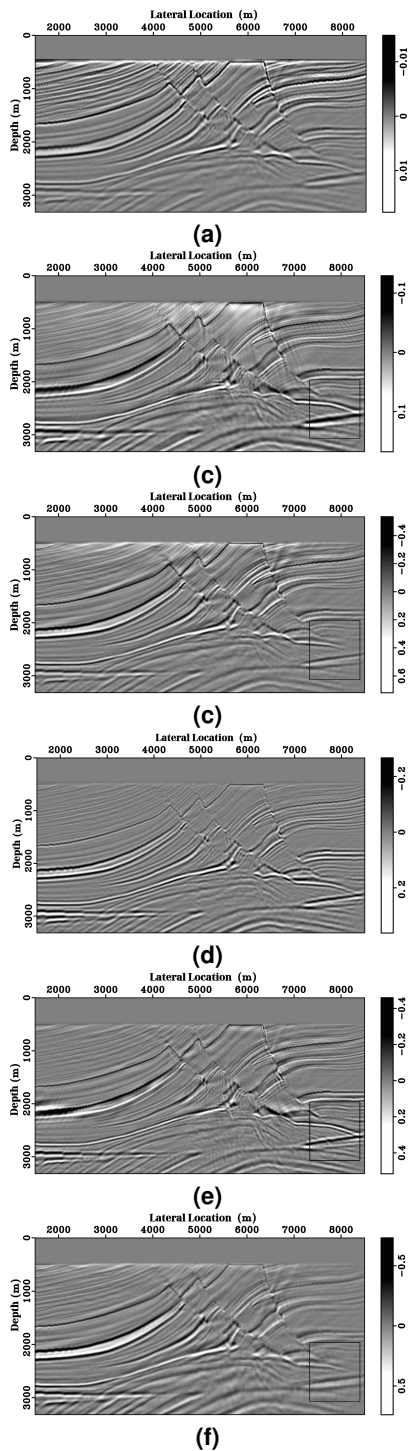

(c)

(d)

(e)

(f)

Figure 2: Results of the LSRTM. (a) RTM image resulting from the conventional image condition (CLI), (b) and (c) results of the conventional ID-LSRTM and DD-LSRTM, respectively. (d) RTM image using ISIC, (e) and (f) results of the ISIC-based ID-LSRTM and DD-LSRTM, respectively.

and seismic velocity models. For this, we compare the performance of the LSRTM and FWI methods based on ISIC with the conventional approaches of these inversion methodologies.

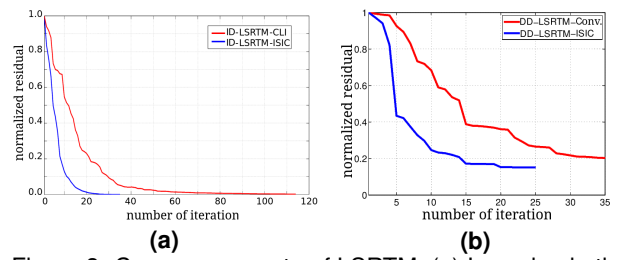The numerical results of the LSRTM using the synthetic

(a)   **(b)**

Figure 3: Convergence rate of LSRTM. (a) Inversion in the image domain using Conjugate Gradient. (b) Inversion in the data domain using LBFGS.
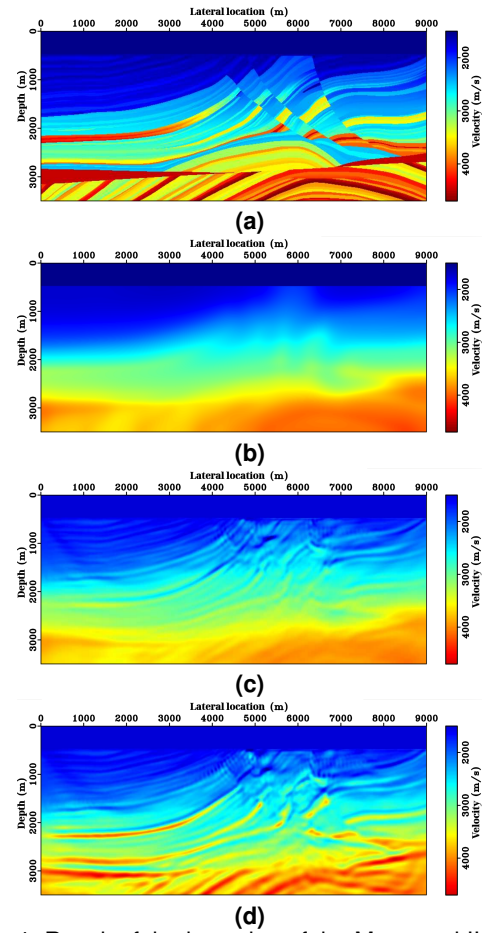

(a)

(b)

(c)

(d)

Figure 4: Result of the inversion of the Marmousi II model. True velocity (a), initial velocity (b), and velocity models retrieved by FWI using conventional FWI preconditioned with the pseudo-Hessian (c) and modified ISIC (d).
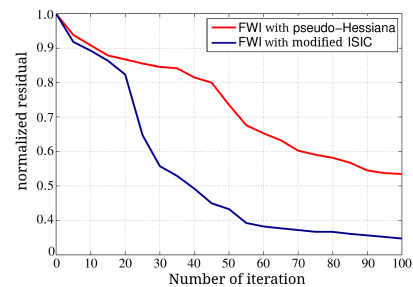

Figure 5: Convergence rate of the FWI objective function.

dataset of the Marmousi II model demonstrated that, in general, the ISIC accelerates the convergence of the optimization algorithm. The formulation using the Laplacian filter and only one cross-correlation term allowed the LSRTM based on ISIC not to require additional costs compared to the conventional LSRTM.

We applied the modified ISIC in the FWI to precondition the inversion with the low wavenumber components of the reflected wavefield. The results obtained from the inversion of the synthetic data from the Marmousi II model showed that this approach recovered a velocity model with higher resolution in the deeper layers compared to the conventional FWI result.

acknowledgments

References

Albano, N. A., J. C. Costa, J. Schleicher, and A. Novais, 2023, On the estimation of reflectivity in reverse time migration: Implementational forms of the inverse-scattering imaging condition: Geophysics, **88**, S1–S16.

Carneiro, M. d. S. R., B. Pereira-Dias, D. M. Soares Filho, and L. Landau, 2018, On the scaling of the update direction for multi-parameter full waveform inversion: Applications to 2d acoustic and elastic cases: Pure and Applied Geophysics, **175**, 217–241.

Claerbout, J. F., 1971, Toward a unified theory of reflector mapping: Geophysics, **36**, 467–481.

——, 1992, Earth soundings analysis: Processing versus inversion: Blackwell Scientific Publications Boston, **6**.

Dai, W., and J. Schuster, 2009, Least-squares migration of simultaneous sources data with a deblurring filter, *in* SEG Technical Program Expanded Abstracts 2009: Society of Exploration Geophysicists, 2990–2994.

Douma, H., D. Yingst, I. Vasconcelos, and J. Tromp, 2010, On the connection between artifact filtering in reverse-time migration and adjoint tomography: GEOPHYSICS, **75**, S219–S223.

Duveneck, E., M. Kiehn, A. Chandran, and T. Kühnel, 2021, Reflection angle/azimuth-dependent least-squares reverse time migration: Geophysics, **86**, S325–S338.

Fletcher, R. P., D. Nichols, R. Bloor, and R. T. Coates, 2016, Least-squares migration—data domain versus image domain using point spread functions: The Leading Edge, **35**, 157–162.

Guitton, A., 2004, Amplitude and kinematic corrections of migrated images for nonunitary imaging operators: Geophysics, **69**, 1017–1024.

Guo, S., and H. Wang, 2020, Image domain least-squares migration with a hessian matrix estimated by non-stationary matching filters: Journal of Geophysics and Engineering, **17**, 148–159.

Kiyashchenko, D., R.-E. Plessix, B. Kashtan, and V. Troyan, 2007, A modified imaging principle for true-amplitude wave-equation migration: Geophysical Journal International, **168**, 1093–1104.

Menke, W., 1989, Geophysical data analysis: Discrete inverse theory: Academic press.

Nemeth, T., C. Wu, and G. T. Schuster, 1999, Least-squares migration of incomplete reflection data: Geophysics, **64**, 208–221.

Op't Root, T. J., C. C. Stolk, and V. Maarten, 2012, Linearized inverse scattering based on seismic reverse time migration: Journal de mathématiques pures et appliquées, **98**, 211–238.

Osorio, L. N., B. Pereira-Dias, A. Bulcão, and L. Landau, 2021, Migration deconvolution using domain decomposition: Geophysics, **86**, S247–S256.

Pratt, R. G., and M. H. Worthington, 1990, Inverse theory applied to multi-source cross-hole tomography. part 1: Acoustic wave-equation method 1: Geophysical prospecting, **38**, 287–310.

Ramos-Martinez, J., S. Crawley, K. Zou, A. Valenciano, L. Qiu, N. Chemingui, and A. Long, 2016, A robust gradient for long wavelength fwi updates: ASEG Extended Abstracts, **2016**, 1–5.

Schuster, G., and Z. Liu, 2019, Least squares migration: Current and future directions: 81st EAGE Conference and Exhibition 2019, European Association of Geoscientists & Engineers, 1–5.

Shin, C., and D.-J. Min, 2006, Waveform inversion using a logarithmic wavefield: Geophysics, **71**, R31–R42.

Sirgue, L., 2006, The importance of low frequency and large offset in waveform inversion: 68th EAGE conference and exhibition incorporating SPE EUROPEC 2006, European Association of Geoscientists & Engineers, cp–2.

Sirgue, L., O. Barkved, J. Van Gestel, O. Askim, and J. Kommedal, 2009, 3d waveform inversion on valhall wide-azimuth obc: 71st EAGE Conference and Exhibition incorporating SPE EUROPEC 2009, European Association of Geoscientists & Engineers, cp–127.

Snieder, R., and J. Trampert, 1999, Inverse problems in geophysics, *in* Wavefield inversion: Springer, 119–190.

Tarantola, A., 1984, Inversion of seismic reflection data in the acoustic approximation: Geophysics, **49**, 1259–1266.

Trad*, D., 2015, Least squares kirchhoff depth migration: Implementation, challenges, and opportunities, *in* SEG Technical Program Expanded Abstracts 2015: Society of Exploration Geophysicists, 4238–4242.

Valenciano, A., S. Lu, N. Chemingui, and J. Yang, 2015, High resolution imaging by wave equation reflectivity inversion: Presented at the 77th EAGE Conference and Exhibition 2015.

Valenciano, A. A., 2008, Imaging by wave-equation inversion: Citeseer, **69**.

Virieux, J., A. Asnaashari, R. Brossier, L. Métivier, A. Ribodetti, and W. Zhou, 2017, An introduction to full waveform inversion, *in* Encyclopedia of exploration geophysics: Society of Exploration Geophysicists, R1–1.

Warner, M., A. Ratcliffe, T. Nangoo, J. Morgan, A. Umpleby, N. Shah, V. Vinje, I. Štekl, L. Guasch, C. Win, et al., 2013, Anisotropic 3d full-waveform inversion: Geophysics, **78**, R59–R80.